

Supporting Information

**High Performance Binary Cross-Linked Alkaline Anion Polymer Electrolyte
Membrane for All-Solid-State Supercapacitors and Flexible Rechargeable Zinc-Air
Batteries**

Min Wang^a, Nengneng Xu^a, Jing Fu^{a,c}, Yuyu Liu^d, Jinli Qiao^{a,b*}

*^aState Key Laboratory for Modification of Chemical Fibers and Polymer Materials,
College of Environmental Science and Engineering, Donghua University,
2999 Ren 'min North Road, Shanghai 201620, P. R. China*

*^bShanghai Institute of Pollution Control and Ecological Security,
Shanghai 200092, P. R. China*

*^cCollege of Materials Science and Engineering, Donghua University,
2999 Ren 'min North Road, Shanghai 201620, P. R. China*

*^dInstitute of Sustainable Energy, Shanghai University,
99 Shangda Road, Shanghai 200444, P. R. China*

*Corresponding author. Tel: +86-21-67792379. Fax: +86-21-67792159.

E-mail: qiaojl@dhu.edu.cn (JLQ)

1. Experimental section

1.1 Materials and fabrication of hydroxide-conductive membrane.

The hydroxide-conductive membranes were fabricated by the following steps. First, the mixture solution was prepared by dissolving PVA (2g) (99% hydrolyzed, average molecular weight $M_w = (146,000-186,000)$, Aldrich) and GG powder (1g) (99%, Usolf) into distilled water (100mL) and then heating it to 90 °C with continuous stirring until a transparent solution was achieved. The resultant solution was poured into plastic Petri dishes and dried at room temperature conditions. Then, the membranes with a thickness range of 30-40 μm were annealed at 140 °C for 1 hour and afterward were immersed in chemical cross-linker solutions: 10 wt% GA (50 wt% solution in H_2O , J&K Scientific) and GA-PCL (10 wt%) (98%, J&K Scientific) with GA: PCL being 1:5 by volume for 2 h, respectively. At last, the obtained membrane was hydroxide-exchanged from chloride form to the hydroxide one in 2 M KOH solution for 24 h and was washed and soaked in DDI water.

1.2 Fabrication of all-solid-state SCs and electrochemical characterization.

The all-solid-state SCs was assembled in a sandwich-like configuration of working electrode//membrane//working electrode. A homogeneous activated carbon ink was coated onto Ti foils and dried under ambient temperature to form the working electrodes with a loading of 2 mg cm^{-2} . All the electrochemical tests were measured using a CHI 660D (Shanghai, China) electrochemical workstation. Cyclic voltammetry (CV), galvanostatic charge and discharge (GCD), and EIS measurements were carried out. The EIS tests were performed in potential amplitude of 5 mV and frequency range of 0.1Hz to 100 kHz. The mass specific capacitance (C, F/g) of all-solid-state SCs was obtained from the GCD curves according to the formula¹:

$$C = \frac{I \times \Delta t}{m \times \Delta V} \quad (\text{S1})$$

The energy density (E, Wh kg⁻¹) and power density (P, kW kg⁻¹) of the all-solid-state SCs were evaluated according to the following equations:

$$E = \frac{C \times \Delta V^2}{2} \quad (\text{S2})$$

$$P = \frac{E}{\Delta t} \quad (\text{S3})$$

where I, Δt , m, ΔV are the discharge current (A), the time duration for a full discharge (s), the total mass (g) of active materials on two electrode, and the actual voltage excluding voltage drop (IR) (V) on discharge, respectively.

1.3 Fabrication of all-solid-state zinc-air battery and electrochemical characterization.

A rechargeable zinc-air battery was constructed through a layer-by-layer method, where the polished zinc foil was employed as the anode, membrane was used as solid-state electrolyte and the air electrode was fabricated by applying IrO₂ and 40 wt% Pt/C (Johnson Matthey) as bi-functional electroactive material. The Catalyst ink consisted of IrO₂/ Pt/C (1:1 by mass), 5 wt % Nafion and ethanol was doctor bladed onto a carbon cloth with a catalyst loading of 2.0 mg cm⁻². The zinc-air battery electrochemical measurements were carried out at ambient conditions. The Polarization data was obtained by utilizing galvanodynamic method. Galvanostatic discharge was performed at constant current density. The charge-discharge cycling test was measured by a galvanic pulse method at a fixed current density.

2. Physical characterization and measurement

2.1 Characterization.

The morphology of the membrane were characterized by atomic force microscope (AFM) (Agilent5500), small angle X-ray scattering (SAXS) (SAXSess mc², Anton Paar) and scanning electron microscopy (SEM) (S-4800, Japan). FT-IR spectra (FTIR) (Tensor 27, Bucker) was used to analyze the chemistry structure of the membrane.

2.2 Water uptake (WU) and swelling ratio (SR).

The samples were immersed in deionized water for 24 h at room temperature. After water on the membrane surface was removed, the weight and dimension were detected immediately. Then, the samples were vacuum dried at 60 °C for 24 h. The WU and SR including in-plane (I-SR) and through-plane (T-SR) calculation followed:

$$WU(\%) = \frac{W_w - W_d}{W_d} \times 100 \quad (S4)$$

$$I - SR(\%) = \frac{A_w - A_d}{A_d} \times 100 \quad (S5)$$

$$T - SR(\%) = \frac{T_w - T_d}{T_d} \times 100 \quad (S6)$$

where W_w (g), A_w (mm²) and T_w (mm) are the weight, surface area and thickness of fully hydrated membranes, respectively. W_d (g), A_d (mm²) and T_d (mm) are the weight, surface area and thickness of dried membranes, respectively.

2.3 Ionic conductivity.

AC impedance technique was utilized to monitor the OH⁻ conductivity of the membranes at room temperature in the in-plane direction. The completely hydrated membrane samples were sandwiched in Teflon conductivity cell which equips with Pt foil. Throughout the measurements, the membranes brought into contact with water to

prevent CO₂ contamination. The OH⁻ conductivity (σ) was calculated according to the formula.

$$\sigma = \frac{L}{RA} \quad (S7)$$

where L represents the distance (cm) between the two potential electrodes, A is the cross-sectional area of sample (cm²), and R is the detection resistance (Ω).

2.4 Mechanical testing.

The mechanical properties of dry membrane specimens (1cm × 3cm) using the (H5K-S, Hounsfield) were measured at a constant rate of 5mm min⁻¹ under ambient temperature.

2.5 Ion exchange capacity (IEC).

IEC of all the membrane samples in the form of hydroxide was measured by immersing in 40 mL of 0.1 M HCl solution for 24 h, then which was titrated using 0.1 M NaOH solution. The IEC calculation follows the equation:

$$IEC(\text{mequiv/g}) = \frac{M_{O,HCl} - M_{E,HCl}}{W_d} \quad (S8)$$

where M_{O, HCl} (mmol) and M_{E, HCl} are the initial and the residual HCl quantity (monitored by the titration), respectively. W_d (g) is the weight of dry membrane.

2.6 Thermal Stability.

Thermal stability of the membrane was conducted by using a thermogravimetric analyzer (TGA) (TG 209, Netzsch) in a heating rate of 10 °C min⁻¹ in nitrogen with the temperature range from 25 to 600 °C.

2.7 Ion transport number (t_{ion}).

The Wagner's polarization technique^{2, 3} was used to evaluate the ionic transport numbers on a CHI 660D (Shanghai, China) electrochemical workstation. The t_{ion} was calculated according to the equation below:

$$t_{ion} = \frac{I_I - I_f}{I_I} \quad (S9)$$

where I_I is the initial current and I_f is the final residual current, respectively.

2.8 Self-Discharge measurement.

Self-discharge experiment of the PGG-GP-based SCs was carried out by first charging the electrode to a voltage of 1.4 V. Then the open circuit voltage of SCs was conducted using CHI660D electrochemical workstation.

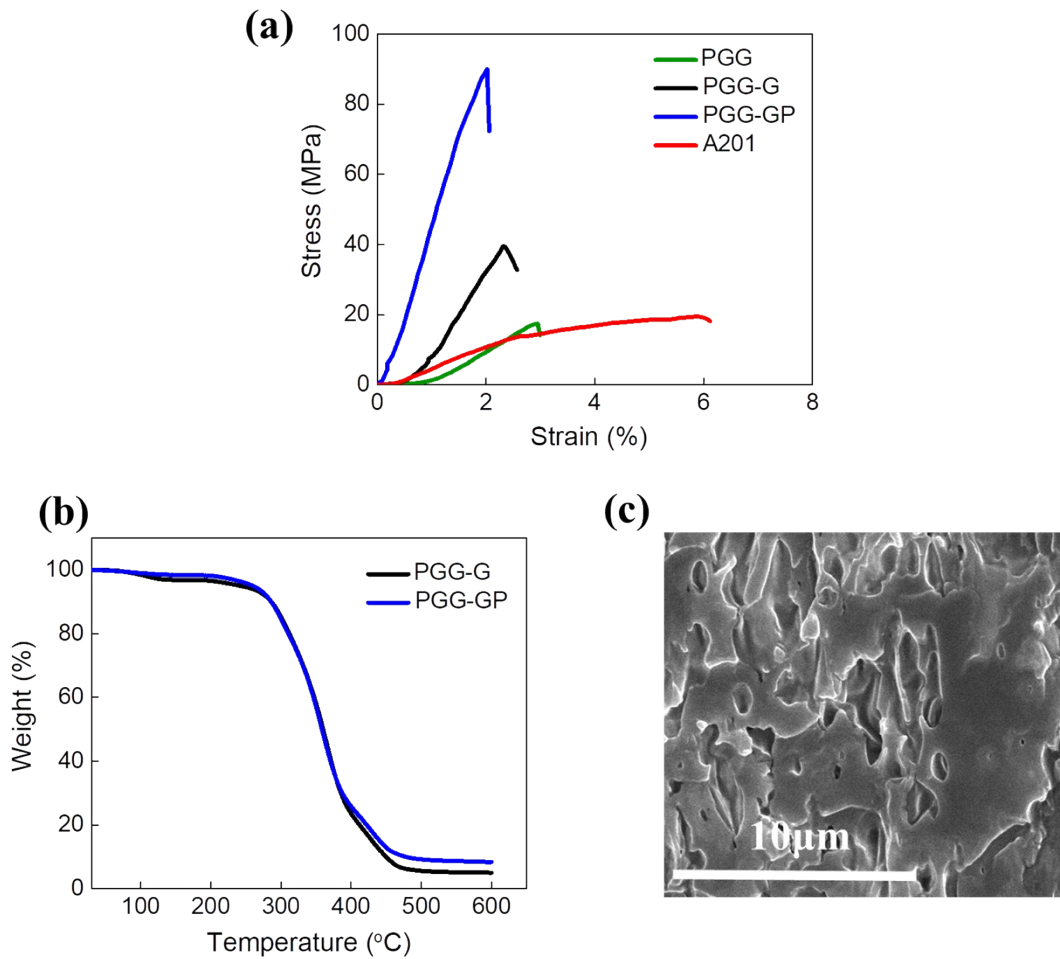


Figure S1 (a) Stress-strain curves of PGG (without cross-linking), PGG-G, PGG-GP, and A201 membranes. (b) TGA thermograms of PGG-G and PGG-GP membranes. (c) The SEM cross-sectional image of the PGG-G membrane.

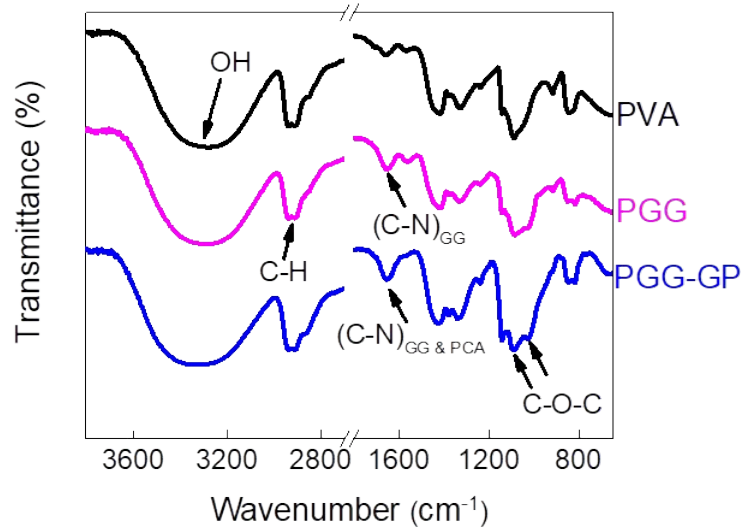


Figure S2 FTIR spectra of PVA, PGG, and PGG-GP membranes.

FT-IR spectra of the PVA, PGG, and PGG-GP membranes are compared in Figure S2. The spectra of PVA displays some common peaks, including O-H stretch vibration of intramolecular and intermolecular hydrogen bonds emerges at $\sim 3271\text{ cm}^{-1}$; the peak at $2921\sim 2941\text{ cm}^{-1}$ is due to the stretching vibration of CH_3 -, CH_2 - and CH - groups. For the PGG membrane, a new peak that appears at $\sim 1651\text{ cm}^{-1}$ corresponds to the bending vibration of C-N group of GG, substantiating GG is effectively incorporated into the PVA matrix. In the spectrum of PGG-GP, two new peaks at ~ 1141 and $\sim 1031\text{ cm}^{-1}$ assigning to C-O-C stretching vibration appear, implying cross-linking reaction between PVA and the aldehyde groups. Additionally, it needs to be emphasized that although there is an overlap of C-N of GG and C-N of PCL at $1620\sim 1670\text{ cm}^{-1}$ in PGG-GP membrane⁴, the intensity of the peak is significantly higher than that of the PGG one. As a result, based on the above facts a binary cross-linking via the acetal reaction is confirmed to occur in PGG-GP membrane.

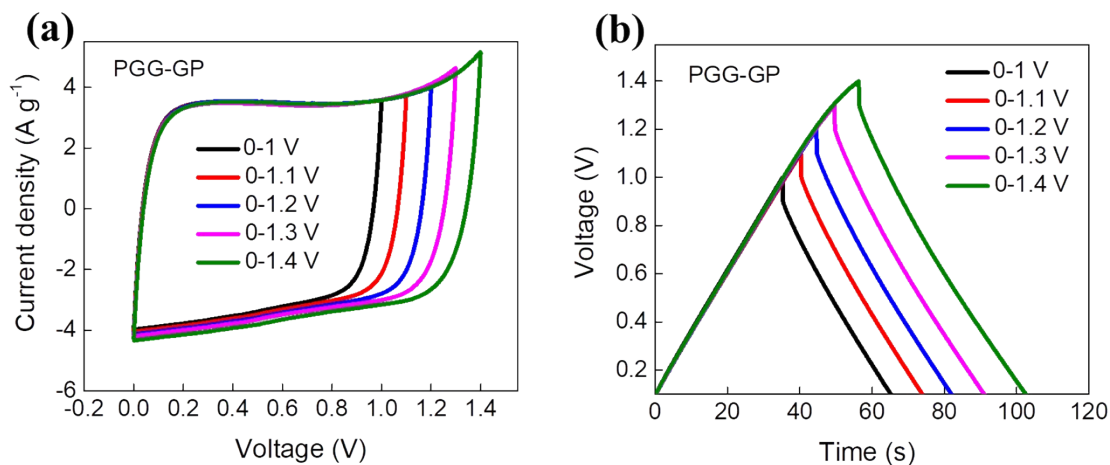


Figure S3 PGG-GP based all-solid-state supercapacitors measured in various potential windows (a) CV curves at 50 mV s⁻¹. (b) GCD profiles at 2 A g⁻¹.

The CV curves and GCD profiles of the all-solid-state supercapacitors comprising of PGG-GP polymer electrolyte in various potential windows are performed at ambient conditions, respectively. The CV curves display approximately rectangular shape (Figure S3a) and GCD profiles show nearly triangular linear behavior (Figure S3b); 1.4 V of a stable potential window is able to be acquired without significant degeneration. As a consequence, the PGG-GP-based supercapacitors exhibits 0-1.4 V of electrochemical stability window.

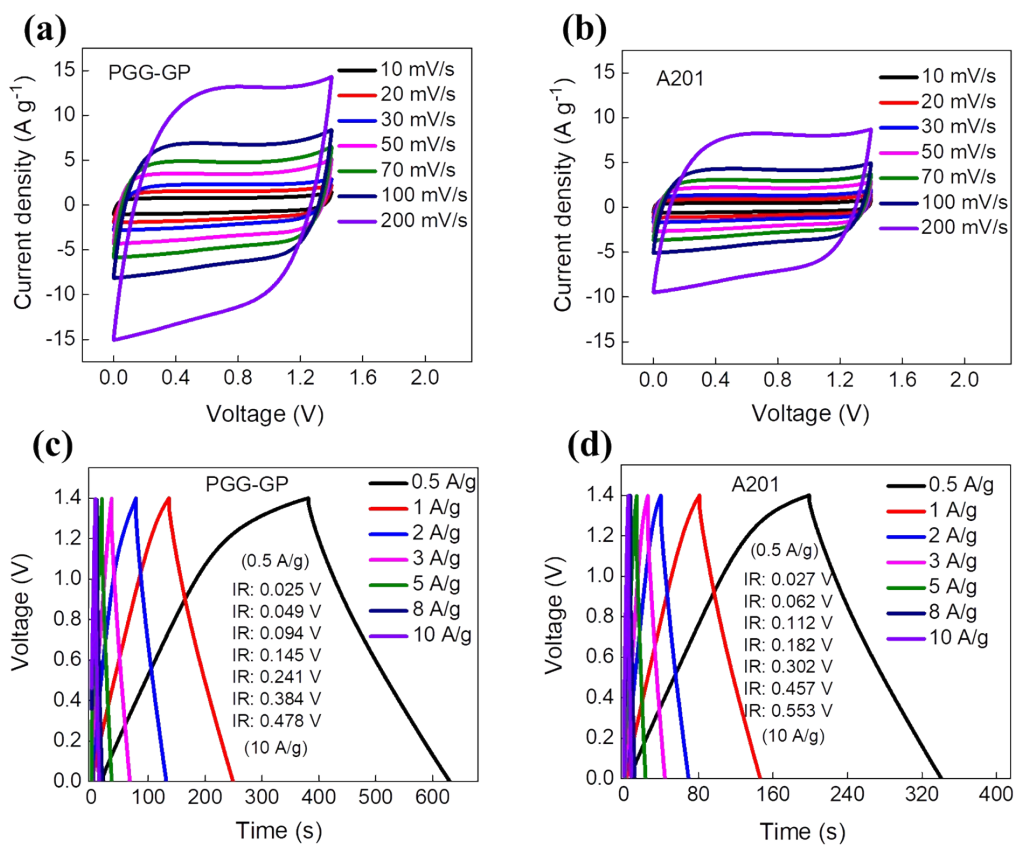


Figure S4 Electrochemical performance of the PGG-GP and A201 membranes based all-solid-state supercapacitors, (a)-(b) CV curves at different scan rates from 10 to 200 mV s⁻¹. (c)-(d) GCD profiles at different current densities from 0.5 to 10 A g⁻¹. Inset shows the voltage drop corresponding to the current density

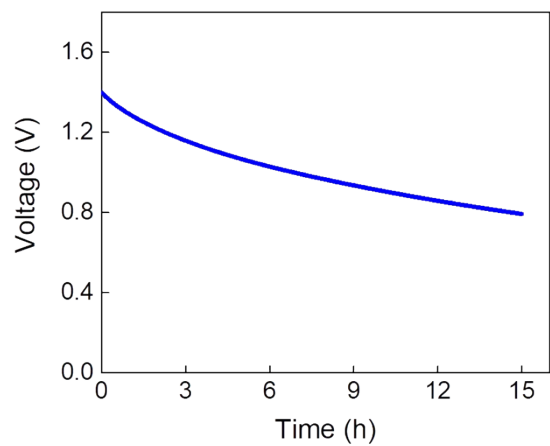


Figure S5 Self-discharge curve of the PGG-GP-based supercapacitors.

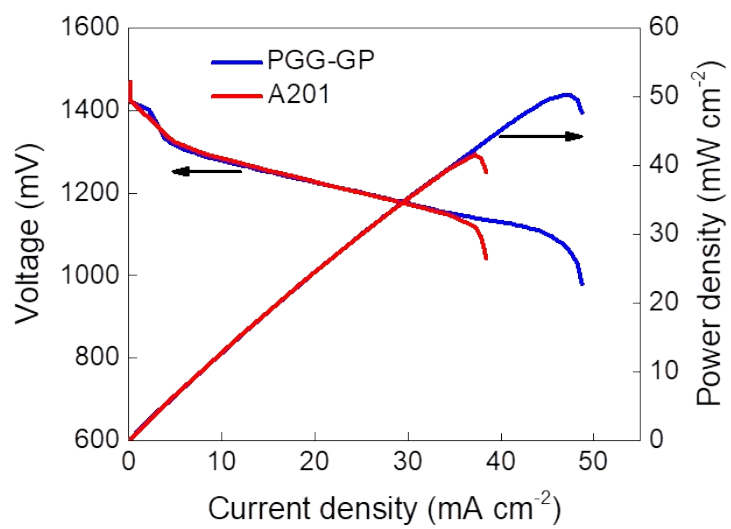


Figure S6 Polarization curves and the corresponding power density plots of the all-solid-state zinc-air battery using PGG-GP and A201 membranes.

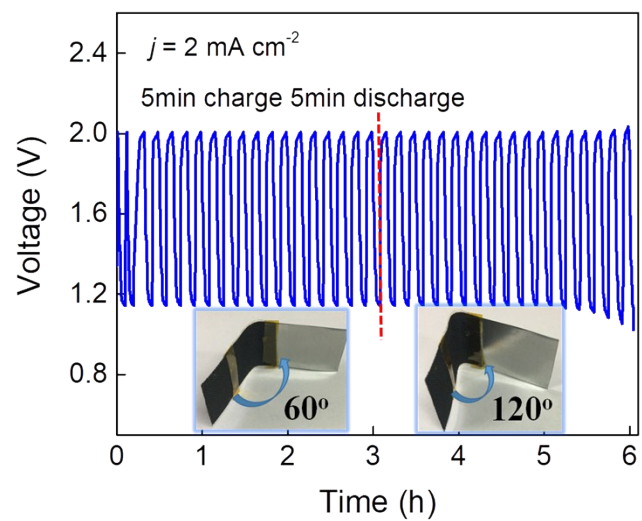


Figure S7 Charge and discharge curve of the zinc-air battery using PGG-GP membrane under bending angles of 60° and 120° .

Table S1. Mechanical properties of PGG, PGG-G, PGG-GP, and A201 membranes.

Samples	Tensile strength at break (MPa)	Young's Modulus (MPa)	Elongation at break (%)
PGG	17.46	870	2.95
PGG-G	39.6	2340	2.32
PGG-GP	90	5343	2.02
A201	19.4	658	5.82

Table S2. Properties of PGG-GP membrane in different anion types at room temperature.

Anion type	Water uptake (g g ⁻¹)	In-plane swelling ratio (%)	Through-plane swelling ratio (%)	Anisotropic swelling degree	Conductivity (S cm ⁻¹)
OH ⁻	1.40	15.2	22.8	1.5	0.123
CO ₃ ²⁻	1.45	13.4	18.8	1.4	0.112

Table S3. Hydroxide conductivity of alkaline anion exchange membranes.

Membrane	Temperature (°C)	Conductivity (S cm ⁻¹)	Reference
QAFCGO	r.t.	0.0333	5
2-QAFC	r.t.	0.0212	6
CS-PDDA-OH ⁻	r.t.	0.024	7
PVA/PDDA-HM _w	r.t.	0.027	8
a ₅ -QAPS	r.t.	0.028	9
PVA/PDDA-OH ⁻	r.t.	0.025	10
PGG-GP	r.t.	0.123	This work

Table S4. Comparison of mass specific capacitance (C) of the PGG-GP-based SC_s with some other carbon-based SC_s.

Electrode material	Loading mass (mg cm ⁻²)	Electrolyte	Test condition	C (F/g)	Reference
CNTs	2	CS-PDDA	1.0V, 100 mV/s	7.49	7
Activated carbon	--	PAMPS/MMT	1.0 V, 0.01A/g	22	11
Activated carbon	--	PEGMA/PEGDMA/ P ₁₃ FSI	2.5 V, 0.5A/g	<25	12
CNT-graphite	1.5	CS-PAADDA-OH ⁻	1.2V, 100 mV/s	2.73	13
Activated carbon	2	PGG-GP	1.4V, 0.5A/g	45.2	This work
Activated carbon	2	PGG-GP	1.4V, 10A/g	33.9	This work

References

1. M. Jin, Y. Zhang, C. Yan, Y. Fu, Y. Guo and X. Ma, *ACS Appl. Mater. Interfaces*, 2018, DOI: 10.1021/acsami.8b00083.
2. J. B. Wagner and C. Wagner, *J. Chem. Phys.*, 1957, **26**, 1597-1601.
3. J. Qiao, N. Yoshimoto, M. Ishikawa, and M. Morita, *Chem. Mater*, 2003, **15**, 2005-2010.
4. G. Bergamaschi, A. Bonardi, E. Leporati, P. Mazza, P. Pehzgatti, C. Pelizzi, G. Pelizzi, M. C. Rodriguez Argiuelles and a. F. Zuni, *J. Inorg. Biochem.*, 1994, **68**, 295-305.
5. J. Zhang, J. Fu, X. Song, G. Jiang, H. Zarrin, P. Xu, K. Li, A. Yu and Z. Chen, *Adv. Energy Mater.*, 2016, **6**, 1600476.
6. J. Fu, J. Zhang, X. Song, H. Zarrin, X. Tian, J. Qiao, L. Rasen, K. Li and Z. Chen, *Energy Environ. Sci.*, 2016, **9**, 663-670.
7. Y. Wei, M. Wang, N. Xu, L. Peng, J. Mao, Q. Gong and J. Qiao, *ACS Appl. Mater. Interfaces*, 2018, **10**, 29593-29598.
8. J. Zhang, T. Zhou, J. Qiao, Y. Liu and J. Zhang, *Electrochim. Acta*, 2013, **111**, 351-358.
9. J. Han, J. Pan, C. Chen, L. Wei, Y. Wang, Q. Pan, N. Zhao, B. Xie, L. Xiao, J. Lu and L. Zhuang, *ACS Appl. Mater. Interfaces*, 2018, DOI: 10.1021/acsami.8b09481.
10. J. Qiao, J. Zhang and J. Zhang, *J. Power Sources*, 2013, **237**, 1-4.
11. J. Wang, X. Yu, C. Wang, K. Xiang, M. Deng and H. Yin, *J. Alloys Compd.*, 2017, **709**, 596-601.
12. V. Chaudoy, F. Tran Van, M. Deschamps and F. Ghamouss, *J. Power Sources*, 2017, **342**, 872-878.
13. B. Ao, Y. Wei, M. Wang, Y. Cai, K. Lian and J. Qiao, *Electrochim. Acta*, 2018, **276**, 319-324.